Journal of Materials Chemistry A

PAPER

View Article Online
View Journal

Cite this: DOI: 10.1039/c6ta02285e

Novel self-assembled natural graphite based composite anodes with improved kinetic properties in lithium-ion batteries†

Miao Chen,‡[a] Zhoulu Wang,‡[a] Aoning Wang,[a] Weishan Li,[b] Xiang Liu,*[a] Lijun Fu*[c] and Wei Huang[a]

Received 17th March 2016
Accepted 24th May 2016

DOI: 10.1039/c6ta02285e

www.rsc.org/MaterialsA

Novel self-assembled natural graphite composites (SANGs) were prepared by the granulation of natural graphite and styrene/acrylonitrile copolymer (SAN) particles by a spray-drying and subsequent pyrolysis procedure. In this work, monodispersed SAN particles with high residual carbon contents were prepared by the dispersion polymerization of acrylonitrile and styrene using the mixture initiators of 2,2′-azobis(isobutyronitrile) and benzoyl peroxide in the presence of polyvinylpyrrolidone in ethanol. The morphology and structure of SAN particles and SANGs were characterized by scanning electron microscopy (SEM), high resolution transmission electron microscopy (HRTEM), X-ray diffraction (XRD) and Raman spectroscopy. The residual carbon contents and the pyrolytic carbon composition of SAN particles were characterized by thermogravimetric analysis (TGA) and X-ray photoelectron spectroscopy (XPS). The as-prepared SANGs present more improved kinetic properties than those of natural graphite when used as anodes in Li-ion batteries. It is due to the self-assembled morphology of SANGs, which improves the less anisotropic transport of Li ions and facilitates the electrochemical kinetics during cycling.

1. Introduction

It is well known that acrylonitrile-based polymers have been used as precursors for preparing carbon materials with desirable surface functional groups and graphite-like structures, which are achieved by the carbonization of these polymers at high temperature.[1,2] In recent years, they have been widely used and studied in surface modifications of nanocomposites, in particular electrode materials for Li-ion batteries. In general, polyacrylonitrile (PAN) or acrylonitrile-rich copolymers with high carbon yields are coated onto electrode particles as precursors,[3,4] and then calcinated at high temperatures to form graphite-like carbonaceous layers that protect the electrode active material from electrochemical side reactions with the electrolyte, prevent the surface oxidation of active materials in air, and improve the conductivity of the composite electrodes.[5–7] Therefore, a large number of research studies on Li-ion batteries have focused on developing active electrode materials with carbonaceous shells derived from PAN or acrylonitrile-rich copolymer precursors for high chemical and electrochemical stability. The role of carbon coatings in different kinds of active materials has been widely studied. For example, PAN has been used as a carbon precursor for sulfur/PAN nanocomposites (SPANs) in which the sulfur chains are chemically bound to the conjugated carbon backbones formed by the pyrolysis of PAN; SPANs are thermally stable at 450 °C, providing a very stable capacity retention and exceptional stability on extended cycling.[8–12] Similarly, polyacrylonitrile block copolymers are anchored onto anatase TiO_2 nanorods as a carbon coating formed by pyrolysis. It is shown that the introduced coating enables a significantly enhanced electrochemical performance of anatase TiO_2 nanorods as anode materials in Li-ion batteries.[13–15]

Additionally, PAN-coated Si nanoparticles are heat-treated under argon to generate a Si/C core–shell nanocomposite as an anode material for Li-ion batteries.[16–18] The conductive carbon shell can not only protect the silicon nanoparticles from aggregation during cycling, but also significantly enhance the capacity retention of the silicon-based anodes. The importance of carbon coating on the silicon surface has been examined in detail by using FT-IR and X-ray photoelectron spectroscopy.[19,20] Kwon *et al.* observed that the absence of a native oxide layer on the silicon surface was prevented by carbon coating.[21]

[a]Key Laboratory of Flexible Electronics (KLOFE), Institute of Advanced Materials (IAM), National Jiangsu Synergistic Innovation Center for Advanced Materials (SICAM), Nanjing Tech University (Nanjing Tech), 30 South Puzhu Road, Nanjing, 211816, China. E-mail: iamxliu@njtech.edu.cn; Tel: +86-025-83587982

[b]School of Chemistry and Environment, South China Normal University, Guangzhou 510006, China

[c]College of Energy and Institute for Electrochemical Energy Storage, Nanjing Tech University (Nanjing Tech), 30 South Puzhu Road, Nanjing, 211816, China. E-mail: l.fu@njtech.edu.cn; Tel: +86-025-58139661

† Electronic supplementary information (ESI) available. See DOI: 10.1039/c6ta02285e

‡ These two authors contributed equally to this work.

In addition to these examples, many efforts have been made in the investigation of carbon coating on natural graphite spheres for Li-ion batteries. Zhang *et al.* directly observed the difference in the SEI formation between carbon coated and non-coated graphite anodes. The result is that the direct contact of graphite with the electrolyte is prevented by using carbon-coated graphite spheres; thus, the decomposition of propylene carbonate is greatly reduced.[5] Moreover, PAN is *in situ* encapsulated on the surface of natural graphite spheres by radiation-initiated polymerization. The modified graphite spheres show obvious improvement in electrochemical performance such as initial coulombic efficiency, cycle ability, and structural stability.[22]

Despite its commercial success and low cost, the application of natural graphite as an anode in Li-ion batteries as a source of electricity for power tools and electromobiles is still quite limited because the highly oriented crystalline nature of natural graphite exhibits strong anisotropic transport properties which cause poor charge/discharge rate performance and limit the lifetime of the batteries.[23,24]

In this work, in order to solve this problem of natural graphite, we report novel self-assembled natural graphite based composite electrode materials (SANGs) with a spherical shape. As illustrated in Fig. 1, the SANGs were prepared by the granulation of natural graphite and SAN particles *via* a spray-drying and subsequent pyrolysis procedure at high temperature. We present that the acrylonitrile-rich SAN particles not only have narrow size distributions, but also have high carbon yields after pyrolysis. The SANGs show improved electrochemical kinetics and rate performance in comparison with those of non-treated natural graphite when used as anodes for Li-ion batteries.

2. Experimental

2.1 Materials

Styrene (St) and acrylonitrile (AN) (Sigma Aldrich, American) were purified by distillation under vacuum. Both of them were stored in the refrigerator before use. Polyvinylpyrrolidone (PVP) (M_{wt} = 36 000 g mol^{-1}; Merck Chemical, Germany) was dissolved in ethanol. 2,2′-Azobis(isobutyronitrile) (AIBN) (Merck Chemical, Germany) and benzoyl peroxide (BPO) (Merck Chemical, Germany) were purified by recrystallization. Natural graphite (NG) (Lanzhou Co., Ltd., China) and hydroxymethyl cellulose (CMC) (Landoil Chemical Group Co., Ltd, China) were used without purification.

2.2 Preparation of SAN particles

First, PVP was dissolved in ethanol in a 500 mL four-neck flask equipped with a refluxing condenser and heated in a magnetically stirred water bath at 75 °C under N_2 atmosphere. The initiators were dissolved in monomers (St and AN) and then added into the above flask, maintained at 75 °C for 24 h. The obtained particles prepared by the dispersion polymerization of St and AN were named as SAN particles. The denotation of SANxx indicates SAN particles prepared using both St and AN as monomers with a weight ratio of (100−xx):xx. The polymerization reaction conditions are listed in Table 1.

2.3 Preparation of SAN/NG composites

The NG and SAN particles were used to prepare SAN/NG composites through a spray-drying process. Typically, the CMC aqueous solution was obtained by dissolving CMC in distilled water in a weight ratio of 1 : 100. Then, NG was slowly added to the CMC aqueous solution at high shear rates and kept for 30 min. SAN particles dispersed in ethanol solution were dropped into the above system, and then stirred until a uniformly and finely dispersed mixture (the weight ratio of NG : SAN70 : CMC = 100 : 35 : 0.1) is formed. Finally, the SAN/NG composites were prepared by spray-drying under the following conditions: the air inlet temperature was 280 °C; the outlet temperature was 120 °C; the rotation speed of the centrifugal atomizer was 35 000 rpm; and the rate of suspension delivery was 15 mL min^{-1}.

2.4 Pyrolysis of SAN/NG composites and SAN70 particles

The SAN/NG composites were pyrolyzed in three steps in a quartz tube oven under Ar. First, the SAN/NG composites were heated at 350 °C with a heating rate of 2 °C min^{-1} and kept for 4 h. Then, the temperature was increased up to 500 °C with a heating rate of 1 °C min^{-1} and kept for 3 h. Finally, the temperature was increased up to 900 °C at a heating rate of 2 °C

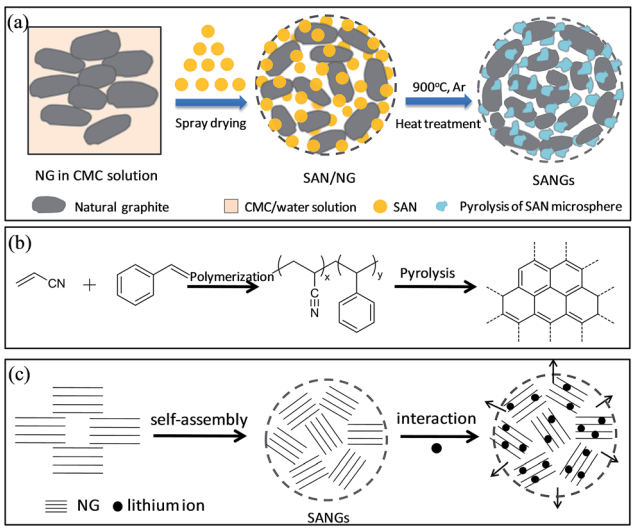

Fig. 1 (a) The preparation of the SANGs; (b) synthetic scheme for the pyrolysis of SAN particles; and (c) the mechanism of intercalation and de-intercalation of Li ions in SANGs.

Table 1 Standard recipe for the dispersion polymerization of St and AN[ab]

Ingredients	Weight/g
Monomer	50.000
PVP	6.174
AIBN	0.325
BPO	0.375
Ethanol	132.726

[a] The ratio of St and AN = 7 : 3. [b] In a sealed four-neck flask, N_2, 75 °C, tumbling speed 30 rpm, 24 h.

min^{-1} and kept for 3 h. The resulting composite was called the SANG. The SAN70 particles were also treated by the aforementioned process, and the resulting product is denoted as SAN70-900.

2.5 Characterization

The morphology of the as-prepared particles was observed by SEM (JSM-6360LV). The average diameter of the particles was calculated by counting 100 individual particles using the average diameter analysis software (Nano Measure) from the SEM images. The microstructure of the SANGs was observed by HRTEM (Tecnai G2 F30 S-Twin). Specific surface areas of the samples were obtained from the N_2 adsorption/desorption isotherms using multipoint BET (BELSORP-MINI). X-ray photoelectron spectra were measured by using an XPS (PHI 5000 VersaProbe) equipped with Al Kα radiation (1486.6 eV). XRD was measured with a SmartLab diffractometer equipped with a 9 kW rotating anode Cu source at 40 kV and 200 mA, from 10 to 90° with a scan rate of 0.2° s^{-1}. Raman measurements were performed with a Horiba HR 800 spectrometer with wavelengths of 514.5 nm. TGA was carried out in the temperature range of 100 to 750 °C with an STA409 instrument with a heating rate of 10 °C min^{-1} under N_2 atmosphere.

2.6 Electrochemical measurement

Electrochemical tests of the electrode materials were performed using half-cells with SANGs as the working electrode and lithium metal as the counter electrode. The working electrodes were prepared by mixing 80 wt% active materials (SANGs, heat treated at 900 °C), 10 wt% acetylene black (AC), and 10 wt% polyvinylidene fluoride (PVDF) dissolved in *N*-methyl-2-pyrrolidone (NMP) solution. The electrode slurry was spread thinly onto a copper foil. After carefully drying under vacuum at 60 °C for 12 h, the copper foil was punched into the wafer. The average mass loading of the electrodes was 4.01 mg. Coin cell batteries (CR2430) were assembled in an argon-filled glove box by using the electrolyte of 1 M $LiPF_6$ in a mixture of EC/DEC/EMC (1 : 1 : 1 by volume). Cyclic voltammograms (CV) were measured with an electrochemical workstation (mode CHI660C) at a scanning rate of 0.05 mV s^{-1}. The cycling performance of these cells was tested in a voltage window of 0.01–1.5 V *versus* Li/Li$^+$ at a constant current density of 100 mA g^{-1} at 25 °C. The electronic conductivity of SANGs and NG was investigated by four-point probe measurements. 89 wt% active materials were mixed with 11 wt% PVDF dissolved in NMP solution and the formed homogeneous gel was vacuum dried at 100 °C for 24 h. Then the above mixtures were ground and pressed into pellets under a pressure of 15 MPa with a diameter of 10 mm and thickness of 2.0 and 2.1 mm for NG and SANGs, respectively.

3. Results and discussion

3.1 Effect of monomer concentration and ratios

The SAN particles are prepared with different St and AN ratios of 70/30, 60/40, 50/50, and 40/60 in an ethanol medium in the presence of PVP as a polymeric dispersant. Fig. 2 shows the effects of weight ratios of St to AN in monomer feed on the dispersion copolymerization of St and AN by using the SEM micrographs of the SAN particles. It is seen clearly from Fig. 2 that the sizes of the SAN particles are strongly influenced by the feed ratio of St to AN, namely, the particle size decreases with the increase of the AN content in the monomer feed. This can be explained by the fact that the critical chain length of hydrophobic styrene-rich oligomeric radicals is much shorter than that of hydrophilic acrylonitrile-rich oligomeric radicals resulting from the aggregation of styrene-rich oligomeric radical chains in a short time. Therefore, the possibility of grafting the PVP dispersant onto styrene-rich particle nuclei decreases, and the rate of aggregation from particle nuclei or smaller size particles increases. As a result, styrene-rich SAN particles are correspondingly larger. On the contrary, the number of aggregated acrylonitrile-rich oligomeric chains in each particle is fewer, resulting in a smaller particle size because aggregation is restrained by the grafting reaction between acrylonitrile-rich oligomeric radicals and PVP radicals.

In addition, the SAN particles obtained are uniform spherical particles with a narrow size distribution for the above-mentioned monomer feed ratios. The coefficient of variation (C_v < 4%, the excellent uniformity) can be calculated by using the later mathematical formulas, and the particle size and C_v are shown in Table 2.[25]

3.2 Effect of initiator concentration and type

The dispersion polymerization of St and AN initiated by using AIBN and BPO as initiators is carried out. It is found that there are significant differences between the particle size distribution and polymerization stability using either BPO or AIBN as the initiator in the same way. Fig. 3a1 indicates that the nanosized primary particles produced with AIBN as the initiator can aggregate with each other in earlier stages at the same time to form agglomerates with uniform shapes and ranges in size,

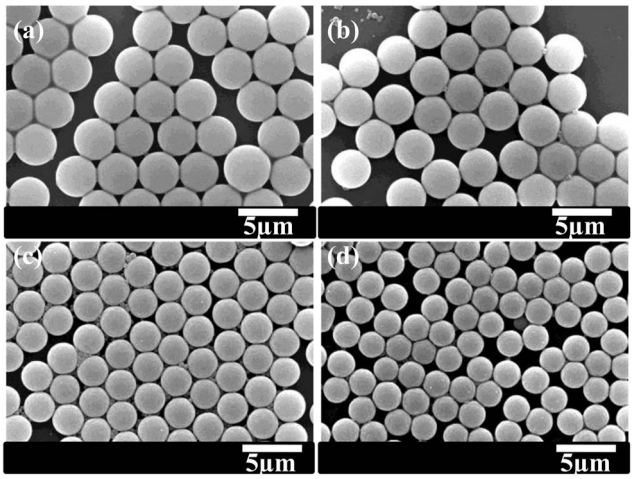

Fig. 2 SEM images of SAN particles synthesized by dispersion polymerization with different monomer weight ratios of St to AN: (a) 70 : 30, (b) 60 : 40, (c) 50 : 50, and (d) 40 : 60.

Table 2 Effect of the AN content on the particle size of SAN microspheres using two different initiators[a]

Sample	St/AN (w/w)	D_n (μm)	C_v[b] (%)
a-SAN30	70/30	3.39	4.37
b-SAN40	60/40	3.26	2.82
c-SAN50	50/50	2.64	3.56
d-SAN60	40/60	2.22	2.83

[a] 1.4% (w/w) mixed initiators relative to monomers; 12.5% (w/w) PVP relative to monomers; 75 °C; 24 h. [b] The coefficient of variation of the number averaged diameter, $D_n = \frac{\sum_{i=n}^{n} D_i}{n}$; standard deviation $= \sqrt{\frac{\sum_{i=1}^{n} (D_i - D_n)^2}{n-1}}$; C_v (%) = (standard deviation)/D_n.

while those produced with BPO as the initiator are retarded to form agglomerates, and thus fewer particles are produced. As a result, the final SAN particles displayed in Fig. 3a2 have a narrow size distribution compared to those prepared with BPO as the initiator in Fig. 3b2.

Therefore, it can be inferred that a more efficient grafting of PVP on SAN particles in the presence of BPO is obtained than that in the presence of AIBN.[26–28] This assumption can also be supported by the fact that the SAN particles obtained by dispersion polymerization with PVP as a polymeric dispersant in an ethanol medium initiated by BPO are more stable than those using AIBN as the initiator, although the particle size distribution of the final SAN particles prepared with BPO as the initiator is quite broad, as shown in Fig. 3b2. On the basis of the above assumption, in order to prepare uniform and stable SAN particles, a mixture of AIBN and BPO initiators in suitable ratios is adopted to establish the balance between aggregation and grafting association in the process of particle formation. It is seen clearly from Fig. 3c1 and c2 that both the agglomerates and the final SAN particles show relatively uniform size distribution and dispersion stability.

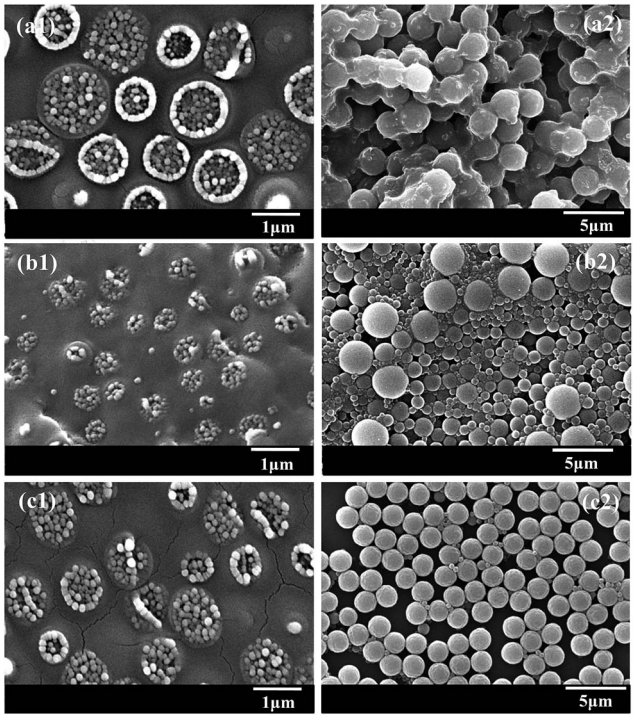

Fig. 3 SEM images of SAN particles (St : AN = 30 : 70 wt%) with different weight ratios of AIBN to BPO: (a1 and a2) 1.4 : 0, (b1 and b2) 0 : 1.4 and (c1 and c2) 0.8 : 0.6 (the left column, 0.5 h; the right column, final products).

3.3 The residual component content analysis

The most important parameter of the SAN particles in applications as electrode materials is the residual carbon content after pyrolysis. TG analysis is used to estimate the residual carbon content of the SAN particles with different ratios of St to AN shown in Fig. 4. It can be clearly seen that the weight loss of the SAN particles occurs at a temperature of about 260 °C, and dramatically decreases at a temperature near 410 °C, which could be ascribed to the pyrolysis of SAN particles. With increasing the temperature up to 500 °C, the residual component basically remains at a constant level which could be ascribed to the carbonization of the SAN particles. The residual component produced by the pyrolysis of SAN70 over the temperature range from 600 to 900 °C is investigated by XPS, and the results are shown in Table 3. It is seen that the residual component consists mostly of carbon and a small portion of nitrogen. Fig. 4 shows that the residual carbon content of the SAN particles increases obviously with increasing monomer feed ratios of AN to St. It can therefore be concluded that the residual component content in the SAN particles depends strongly on the AN content in the feed monomer.

3.4 Morphologies and structures of SANGs

Fig. 5a and b present typical SEM images of the SAN70 and NG particles. In Fig. 5a, the SAN70 particles, corresponding to the

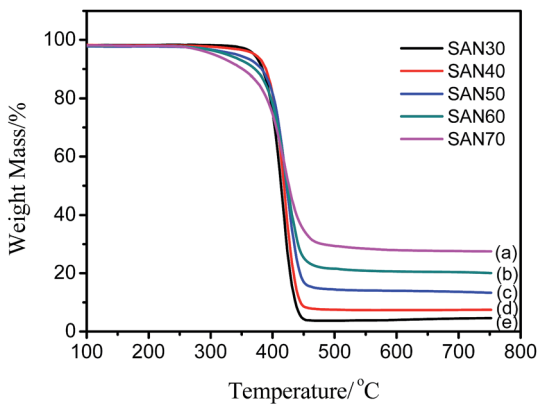

Fig. 4 TGA thermographs of the SAN particles with different weight ratios of St to AN: (a) SAN30, (b) SAN40, (c) SAN50, (d) SAN60, and (e) SAN70, respectively.

Table 3 The atomic composition of the residual component prepared by pyrolyzing SAN70 particles under different temperatures detected by XPS

Sample	Carbon (at%)	Nitrogen (at%)	Nitrogen/carbon
SAN70-600 °C	83.4	16.6	0.20
SAN70-700 °C	83.7	16.3	0.19
SAN70-800 °C	88.3	11.7	0.14
SAN70-900 °C	95.2	4.8	0.05

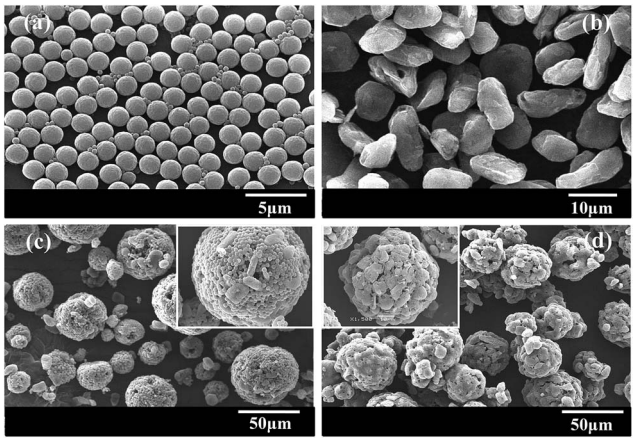

Fig. 5 SEM images of (a) SAN70, (b) NG, (c) SAN70/NG and (d) SANGs.

particles shown in Fig. 3c2 are uniform and stable. In Fig. 5b, NG particles with an average particle size of approximately 8 μm can be observed and the size of the graphite particles is larger than that of the SAN70 particles. Fig. 5c shows the microscopic morphology of the SAN70/NG composites prepared *via* a spray-drying process (shown clearly in the upper-right inset), and their particle size is mostly in the range of 20–50 μm. After the heat treatment, the SANGs are observed by SEM in Fig. 5d, and the spherical particles around the graphite cannot be seen anymore due to the pyrolysis of the SAN70 particles. An enlarged image of SANGs (inset of Fig. 5d) shows the microstructure image of the single SANG particle, which shows the existence of pyrolytic carbon on the surface of NG particles. Different from the NG particles, which prefer exhibiting an ordered orientation with the basal plane upwarded (Fig. 5b), in SANG particles, the NG particles sit less anisotropically in the pyrolytic carbon matrix.[23]

Fig. 6a presents the XRD patterns of NG, SAN70 particles, SAN70/NG composites and SANGs. For NG particles, SAN70/NG and SANGs, the intensity of the sharp peaks at 2θ of approximately 26° is much stronger than that of the rest of the peaks, which is attributed to the lamellar structure of natural graphite. The four peaks located at 40–50° are ascribed to graphite (JCPDS no. 65-6212) and graphite-3R (JCPDS no. 26-1079), while the peaks at 54.6° and 77.6° can be attributed to the diffraction peaks of (004) and (110) of graphite. The XRD pattern of SAN particles shows an obvious broad peak covering a large 2θ range from 10 to 35°, centered at around

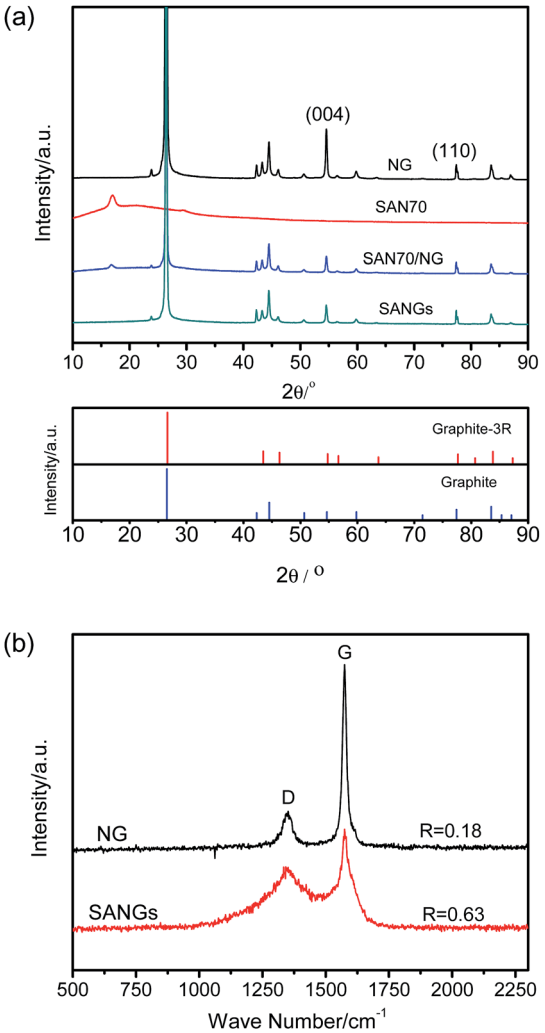

Fig. 6 (a) XRD diffraction patterns of NG, SAN70, SAN70/NG and SANGs; (b) Raman spectra of NG and SANGs.

17°. There is a broad peak of SAN70/NG composites at approximately 17°, which corresponds to the existence of the SAN polymer.[29] However, the above peak disappears in the XRD pattern of SANGs because of the pyrolysis of the SAN70 particles. A degree of orientation is evaluated using an intensity ratio of the (004) peak to the (110) peak (I_{004}/I_{110}).[30] The value of I_{004}/I_{110} of NG particles is 3.81 and that of SANGs is 1.41, from which it is clear that SANGs show less anisotropism than NG.

Fig. 6b shows the Raman spectroscopy of NG particles and SANGs. The two peaks at 1346 cm^{-1} and 1573 cm^{-1} in the spectra of NG particles and SANGs represent the D (disordered carbon) and G (graphite carbon) of graphite, respectively; the D band arises from the disorder induced in sp^2-bonded carbon, whereas the G band arises from the in-plane vibration of the sp^2 carbon atoms of graphene.[31] The ratio of I_D/I_G (denoted as R) is generally used to describe the degree of crystallinity and domain size of the carbon material.[32,33] The R of the SANGs ($R = 0.63$) is dramatically larger than that of NG ($R = 0.18$) due to the presence of the pyrolytic carbon which is derived from SAN70

copolymer particles. A detailed TEM observation of SANGs (Fig. S1†) is in line with the Raman results, confirming a low crystalline degree of the pyrolytic carbon in SANGs. The BET surface areas of SAN70-900, NG and SANGs are 11.29, 8.52 and 3.98 $m^2\ g^{-1}$, respectively. The BET surface area of SANGs is lesser than that of NG particles. The surface area of SANGs decreases due to the aggregation of graphite and pyrolytic carbon.

3.5 Electrochemical properties

Fig. 7a and b display the cyclic voltammetry (CV) curves of NG and SANGs at a scan rate of 0.05 mV s^{-1} in the potential range between 0.01 V and 1.5 V, respectively. For the first cathodic process, a broad peak of SANGs appears in the range of 0.6–1.2 V, and the peak of NG appears in the range of 0.7–1.0 V, which is believed to be responsible for the formation of a solid electrode interface (SEI) film.[34] The above peak disappears in the subsequent cycling, indicating their irreversible feature (see inset in Fig. 7).[35]

The peaks below 0.20 V *vs.* Li^+/Li are related to the Li-ion insertion into graphite. In the anodic process, the peaks below 0.3 V *vs.* Li^+/Li are connected with the de-intercalation behavior of Li ions. In the second cathodic process, three peaks of the NG electrode appear at 0.163, 0.116 and 0.053 V, while those of the SANG electrode appear at 0.176, 0.124 and 0.064 V, which are relatively positive compared to their counterparts for an NG electrode, indicating an easier lithium insertion process into the SANG electrode than into the NG electrode. In the second anodic process, two peaks of the SANG electrode appear at 0.216 and 0.254 V, which show up at a more negative voltage than those for NG electrodes (0.236 and 0.269 V), presenting a faster lithium extraction in SANGs in comparison with NG.

The cycle performance of NG and SANG cells is shown in Fig. 8a. It can be seen that there is no obvious difference between the initial columbic efficiencies of the SANG electrode (88.0%) and those of the NG electrode (89.1%). The first charge capacity of NG and SANG electrodes is 363.2 and 357.7 mA h g^{-1} respectively; after 50 cycles, the reversible capacity of NG and SANG electrode is 361.1 and 348.2 mA h g^{-1}, *i.e.*, 99.4% and 97.3% of that for the first cycle, respectively. The slightly smaller capacity of the SANG electrode is due to the lower capacity contribution of pyrolytic carbon (~270 mA h g^{-1}) in the composites. As seen in Fig. S2,† the pyrolytic carbon presents typical Li-ion insertion/extraction behavior of pyrolytic carbon with a low crystallinity degree, *i.e.*, no obvious charge–discharge plateau observed in the charge–discharge processes, different from those of SANGs.

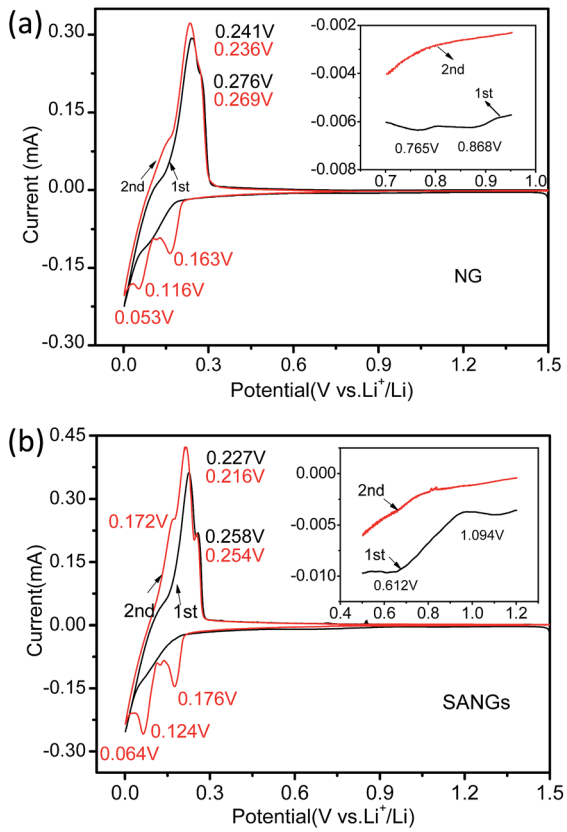

Fig. 7 Cyclic voltammetry characteristics of (a) NG and (b) SANGs in the potential window between 0.01 and 1.5 V at a scan rate of 0.05 mV s^{-1}. Inset: the magnification profiles of cyclic voltammetry profiles in the voltage range of 0.6–1.2 V.

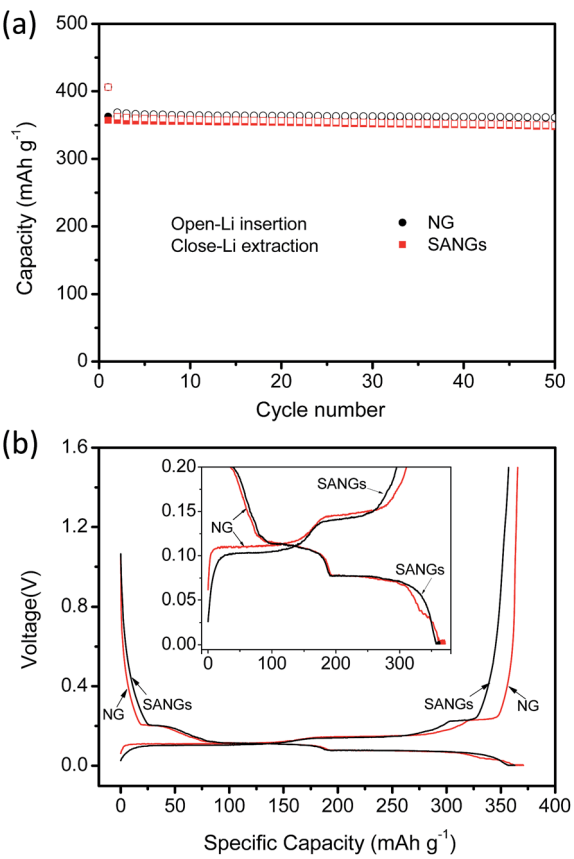

Fig. 8 (a) Cycling performance of NG and SANGs; (b) voltage profiles of NG and SANG electrodes in the second cycle. Inset: the magnification profiles in the voltage range between 0 and 0.2 V.

The charge–discharge curves of both SANGs and NG (Fig. 8b) show typical electrochemical behavior of graphite with several plateaus ascribed to different stages of lithium insertion and extraction,[36] while for the SANGs, at the very beginning of the discharge process, a relatively gentle curve is observed compared with that of NGs, which is due to the capacity contribution of pyrolytic carbon. Besides, the charge plateaus of the SANG electrode (0.09 V and 0.14 V) appear at lower voltages than those of the NG electrode (0.11 V and 0.15 V), which is consistent with the CV results. The location differences of cathodic and anodic peaks and plateaus between NG and SANG electrodes in CV and galvanostatic measurements indicate less polarization in SANG electrodes compared with NG electrodes during charge/discharge processes.

Fig. 9 reveals the rate performance of NG and SANG electrodes at the current densities of 100, 200, 300, 400, 500, 600, 800, and 1000 mA g^{-1}. At the lower current densities of 100 mA g^{-1} and 200 mA g^{-1}, the relatively stable charge capacities of the NG electrode are 364.2 and 337.2 mA h g^{-1}, respectively, while the corresponding charge capacities of SANGs are 356.4 mA h g^{-1} and 333.1 mA h g^{-1}, and slightly lower than those of the NG sample. With the increase of the current density to 300 mA g^{-1}, the SANG electrodes start to deliver a larger capacity (310.0 mA h g^{-1}) than the NG electrode (308.1 mA h g^{-1}). For SANGs, at 500, 600, 800, and 1000 mA g^{-1}, the SANGs deliver a stable charge capacity of 245.4, 214.1, 139.7, and 54.5 mA h g^{-1}, while for NG, the charge capacity remains at 235.7, 202.3, 126.5, and 35.4 mA h g^{-1}, respectively, indicating a better rate performance of SANGs than that of NG.

The electrochemical process during cycling involves both electron and lithium ion transfer. The results from the four-point probe measurements show that the electronic conductivity of SANGs is slightly lower than that of NG (Table S1†), ruling out the possibility that the improved rate performance results from the faster electron transfer of SANGs, while the spherical-shaped structure of SANGs plays an important role, which leads to a decreased anisotropic property of NG in SANGs and facilitates the lithium ion transfer through the edge plane, thus reducing the polarization and enhancing the rate performance.

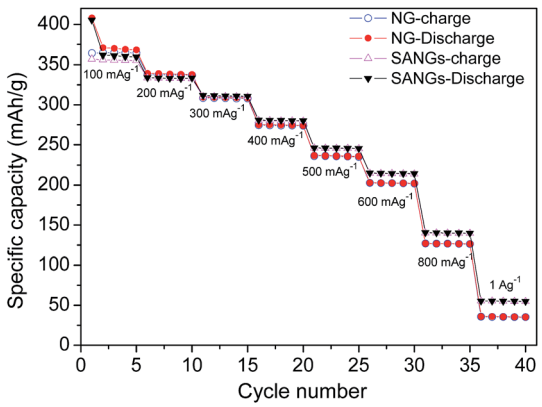

Fig. 9 Rate capacity of NG and SANGs in the potential window between 0.01 and 1.5 V.

4. Conclusions

In this article, SANGs are synthesized by the granulation of NG particles and the pyrolytic carbon derived from SAN particles. The SANGs present a spherical morphology in which NG particles are sitting less anisotropically in the pyrolytic carbon with a random orientation. In this study, monodispersed SAN particles with higher residual carbon contents were prepared by the dispersion polymerization of acrylonitrile and styrene. It is found that the morphology of SAN particles and the stability of the polymer particles during reactions can be efficiently controlled by using a mixture of AIBN and BPO initiators in suitable ratios, using PVP as the polymeric dispersant and ethanol as the medium. The particle size of SAN particles decreases with the increase of the AN content in the monomer feed, and the residual carbon content increases obviously with the increase of the monomer feed ratios between AN and St. The electrochemical results from CV and charge/discharge tests prove that spherical-shaped SANGs show less polarization and better electrochemical kinetics and rate performance in comparison with NG. The enhanced electrochemical performance is attributed to their improved mass transfer properties resulting from the less anisotropic property of natural graphite in SANGs.

Acknowledgements

We thank Prof. Ping He in Nanjing University for electronic conductivity measurements. The research was financially supported from National Natural Science Foundation of China (51502137).

Notes and references

1 M. S. A. Rahaman, A. F. Ismail and A. Mustafa, *Polym. Degrad. Stab.*, 2007, **92**, 1421–1432.
2 W. Zhang, J. Liu and G. Wu, *Carbon*, 2003, **41**, 2805–2812.
3 J. Liu, P. H. Wang and R. Y. Li, *J. Appl. Polym. Sci.*, 1994, **52**, 945–950.
4 P. J. Sánchez-Soto, M. A. Avilés, J. C. del Río, J. M. Ginés, J. Pascual and J. L. Pérez-Rodríguez, *J. Anal. Appl. Pyrolysis*, 2001, **58–59**, 155–172.
5 H. L. Zhang, S. H. Liu, F. Li, S. Bai, C. Liu, J. Tan and H. M. Cheng, *Carbon*, 2006, **44**, 2212–2218.
6 H. Li and H. Zhou, *Chem. Commun.*, 2012, **48**, 1201–1217.
7 Y. C. Yen, S. C. Chao, H. C. Wu and N. L. Wu, *J. Electrochem. Soc.*, 2009, **156**, 95–102.
8 X. G. Yu, J. Y. Xie, Y. Li, H. J. Huang, C. Y. Lai and K. Wang, *J. Power Sources*, 2005, **146**, 335–339.
9 L. Wang, X. M. He, J. J. Li, J. Gao, J. W. Guo, C. Y. Jiang and C. Wan, *J. Mater. Chem.*, 2012, **22**, 22077–22081.
10 J. Fanous, M. Wegner, M. B. M. Spera and M. R. Buchmeiser, *J. Electrochem. Soc.*, 2013, **160**, 1169–1170.
11 J. Fanous, M. Wegner, J. Grimminger, M. Rolff, M. B. M. Spera, M. Tenzer and M. R. Buchmeiser, *J. Mater. Chem.*, 2012, **22**, 23240–23245.

12 J. Fanous, M. Wegner, J. Grimminger, A. Andresen and M. R. Buchmeiser, *Chem. Mater.*, 2011, **23**, 5024–5028.
13 B. Oschmann, D. Bresser, M. N. Tahir, K. Fischer, W. Tremel, S. Passerini and R. Zentel, *Macromol. Rapid Commun.*, 2013, **34**, 1693–1700.
14 F. Nacimiento, J. R. González, R. Alcántara, G. F. Ortiz and J. L. Tirado, *J. Electrochem. Soc.*, 2013, **160**, 3026–3035.
15 L. J. Fu, H. Liu, H. P. Zhang, C. Li, T. Zhang, Y. P. Wu and H. Q. Wu, *J. Power Sources*, 2006, **159**, 219–222.
16 F. D. Liu, Z. L. Wang, Y. J. Zhou and X. Liu, *J. Appl. Polym. Sci.*, 2016, **133**, 43101.
17 H. Zhou, X. Y. Tang, Y. M. Dong, L. F. Chen, L. T. Zhang, W. R. Wang and X. Xiong, *J. Appl. Polym. Sci.*, 2011, **120**, 1385–1389.
18 D. Shao, D. P. Tang, Y. J. Mai and L. Z. Zhang, *J. Mater. Chem. A*, 2013, **1**, 15068–15075.
19 S. Goriparti, E. Miele, F. D. Angelis, E. D. Fabrizio, R. P. Zaccaria and C. Capiglia, *J. Power Sources*, 2014, **257**, 421–443.
20 Y. H. Xu, Y. J. Zhu and C. S. Wang, *J. Mater. Chem. A*, 2014, **2**, 9751–9757.
21 E. Kwon, H. S. Lim, Y. K. Sun and K. D. Suh, *Solid State Ionics*, 2013, **237**, 28–33.
22 K. K. Guo, Q. M. Pan and S. Fang, *J. Power Sources*, 2002, **111**, 350–356.
23 L. J. Song, S. S. Liu, B. J. Yu, C. Y. Wang and M. W. Li, *Carbon*, 2015, **95**, 972–977.
24 L. Zou, F. Y. Kang, X. L. Li, Y. P. Zheng, W. C. Shen and J. Zhang, *J. Phys. Chem. Solids*, 2008, **69**, 1265–1271.
25 J. Lee, J. U. Ha, S. Choe, C. S. Lee and S. E. Shim, *J. Colloid Interface Sci.*, 2006, **298**, 663–671.
26 X. Liu and M. Nomura, *Ind. Eng. Chem. Res.*, 2014, **53**, 17580–17588.
27 X. Liu, F. Mizutani and M. Nomura, *Ind. Eng. Chem. Res.*, 2014, **53**, 664–671.
28 F. Pla, C. Fonteix and H. V. Wal, *Chem. Eng. Technol.*, 2010, **33**, 1859–1876.
29 V. Panwar and R. M. Mehra, *Eur. Polym. J.*, 2008, **44**, 2367–2375.
30 G. E. Bacon, *J. Appl. Chem.*, 1956, **6**, 477–481.
31 M. Su, Z. Wang, H. Guo, X. Li, X. Hang and W. Xiao, *Electrochim. Acta*, 2004, **116**, 230–236.
32 L. Gan, H. J. Guo, Z. X. Wang, X. H. Li, W. J. Peng, J. X. Wang, S. L. Huang and M. R. Su, *Electrochim. Acta*, 2013, **104**, 117–123.
33 M. D. Fang, T. H. Hong, J. P. Yen, Y. R. Lin, J. L. Hong, S. H. Wu and J. J. Jow, *Materials*, 2015, **8**, 3550–3561.
34 J. Zhang, Z. Q. Shi, J. Wang and J. L. Shi, *J. Electroanal. Chem.*, 2015, **747**, 20–28.
35 D. S. Wang, M. X. Gao, H. G. Pan, Y. F. Liu, J. H. Wang, S. Q. Li and H. G. Ge, *J. Alloys Compd.*, 2014, **604**, 130–136.
36 T. Ohzuku, Y. Iwakoshi and K. Sawai, *J. Electrochem. Soc.*, 1993, **140**, 2490–2498.

